

Interpreting the Star Formation Efficiency of Molecular Clouds with Ionising Feedback

Sam Geen^{1,3}★, Juan D. Soler^{2,3}, Patrick Hennebelle³

¹ Zentrum für Astronomie der Universität Heidelberg, Institut für Theoretische Astrophysik, Albert-Ueberle-Str. 2, 69120 Heidelberg, Germany

² Max-Planck-Institute for Astronomy, Königstuhl 17, 69117, Heidelberg, Germany

³ Laboratoire AIM, Paris-Saclay, CEA/IRFU/SAP - CNRS - Université Paris Diderot, 91191, Gif-sur-Yvette Cedex, France

6 May 2022

ABSTRACT

We investigate the origin of observed local star formation relations using radiative magnetohydrodynamic simulations with self-consistent star formation and ionising radiation. We compare these clouds to the density distributions of local star-forming clouds and find that the most diffuse simulated clouds match the observed clouds relatively well. We then compute both observationally-motivated and theoretically-motivated star formation efficiencies (SFEs) for these simulated clouds. By including ionising radiation, we can reproduce the observed SFEs in the clouds most similar to nearby Milky Way clouds. For denser clouds, the SFE can approach unity. These observed SFEs are typically 3 to 10 times larger than the “total” SFEs, i.e. the fraction of the initial cloud mass converted to stars. Converting observed to total SFEs is non-trivial. We suggest some techniques for doing so, though estimate up to a factor of ten error in the conversion.

Key words: stars: massive, stars: formation < Stars, ISM: H ii regions, ISM: clouds < Interstellar Medium (ISM), Nebulae, methods: numerical < Astronomical instrumentation, methods, and techniques

1 INTRODUCTION

In this paper we compare the results of simulations of star forming regions with observationally-derived star formation relations. We focus on the response of star formation efficiencies to the inclusion of ionising radiation emission from massive stars.

Stars form in molecular clouds (see review by Hennebelle & Falgarone 2012). Gas collapses into filaments and cores on the order of a freefall time. In clouds where massive star formation occurs, radiative and mechanical processes drive outflows that resist accretion around the star (see review by Dale 2015). Over time, these processes disperse cloud material and suppress or halt star formation.

Quantifying star formation efficiencies in nearby molecular clouds has been the subject of much study. In one perspective, it has been proposed that star formation rates are well correlated with gas mass (Lada et al. 2010) or surface density Heiderman et al. (2010) above a certain threshold, and that below this threshold the star formation rate is negligible. In a competing view proposed by Gutermuth et al. (2011), Σ_{SFR} is proportional to Σ_{gas}^2 . Hony et al. (2015) argue that in practice distinguishing between these two arguments is difficult due to the steepness of the relations and low

number statistics. The existence of a threshold for star formation has been discussed by Myers & Benson (1983); Beichman et al. (1986), who use $n_{\text{H}} = 10^4 \text{ cm}^{-3}$, whereas Onishi et al. (1998); Johnstone et al. (2004) use $N_{\text{H}} = 10^{22} \text{ cm}^{-2}$, equivalent to the limits found by Lada et al. (2010); Heiderman et al. (2010).

There are various discussions as to why there should be a density criterion for star formation. André et al. (2010) argue that the presence of dense filaments is required for dense star-forming cores, which sets a density criterion for core formation. Burkert & Hartmann (2013) argue that the density threshold for star formation is not a single value, but rather represents gas in which self-gravity has begun to dominate. Lee & Hennebelle (2016) characterise the transition from the diffuse cloud to dense protocluster gas as a transition from infalling material to a virialised structure globally supported by a combination of turbulence and rotation.

Krumholz et al. (2012) argue that the star formation rate is in fact correlated to the local free-fall time, which is set by the volumetric density, not the column density. Clark & Glover (2014) analyse simulation results and find no correlation between the column and volume density of gas, the latter of which sets the star formation rate. They do, however, find a link between the observed column density and the effective column density seen by the star. The link between observed star formation relations and the theory of star formation on small scales is still an open question.

★ Corresponding author: Sam Geen (sam.geen@uni-heidelberg.de)

The picture of star formation is complicated by the introduction of feedback cycles driven by energetic stellar events. In particular, a great deal of attention has been given to the role of ionising feedback. Numerical simulations by Dale et al. (2005); Gritschneider et al. (2009); Peters et al. (2010); Walch et al. (2012); Dale et al. (2012) confirm that ionising UV photons are able to drive outflows in molecular clouds that disperse the supply of dense gas during star formation events. Authors such as Whitworth (1979); Matzner (2002); Krumholz et al. (2006); Goldbaum et al. (2011); Kim et al. (2016) have constructed (semi-)analytic models including radiation feedback to study star formation efficiencies in clouds. One such model by Matzner (2002) find that $10 \pm 5\%$ of the mass in clouds is converted to stars before ionising radiation disperses the cloud.

In our previous work (Geen et al. 2015, 2016), we focussed on the link between simulations and analytic theory. Despite the complexity of the environments, we were successful in reproducing the quantitative behaviour of simple simulated HII regions with analytic theory (Spitzer 1978; Dyson & Williams 1997; Hosokawa & Inutsuka 2006; Raga et al. 2012; Tremblin et al. 2014). We were also able to explain the evaporation of dense clumps in our simulations using the models of Bertoldi & McKee (1990). By comparison, in this work we wish to link our simulations to observed clouds. We compare both the gas structure in observed clouds and the star formation efficiencies. The former is important because our initial conditions are highly idealised, and we cannot be certain how relevant our simulation results are to observed star-forming clouds otherwise.

The goal of this paper is to compare the results of observational studies of local clouds with projections of simulated star forming regions. In particular we wish to understand how ionising radiation sets star formation relations in simulations, and provide insight into how observed star formation efficiencies are obtained. We focus on the relation of Lada et al. (2010), who measure total Young Stellar Object (YSO) numbers and gas masses. By comparison, Heiderman et al. (2010) use surface densities, which we cannot reproduce accurately with our limited YSO mass resolution.

In Section 2 we introduce the simulations used in this study. In Section 4 we discuss our results. We begin by discussing the post-processing techniques used to approximate observations of our simulated clouds. We then present the total star formation efficiency of the clouds over their lifetime. We extend this to an estimate for the observed star formation efficiency of these clouds. We analyse the density distribution of these clouds in comparison to local clouds, and estimate the likelihood of observing each cloud at each point over its lifetime. We then discuss the implications of our study, and some of the limitations of our techniques.

2 NUMERICAL SIMULATIONS

In this section we review the simulations used in this paper. We simulate a set of isolated turbulent molecular clouds with sink particles representing clusters of stars. These particles emit ionising photons that heat the gas they encounter. We use the radiative magneto-hydrodynamic Eulerian Adaptive Mesh Refinement (AMR) code RAMSES (Teyssier 2002; Fromang et al. 2006; Rosdahl et al. 2013).

2.1 Initial Conditions

We run simulations of four clouds with varying mean density, each with initial gas mass $10^4 M_\odot$. These clouds are labelled “L”, “M”, “S” and “XS”, in increasing order of initial compactness.

We summarise these initial conditions in Table 1. The last three clouds have identical initial conditions to the Fiducial, More Compact and Most Compact clouds in Geen et al. (2015). Cloud L is included in this work to increase the range of the study. The total box length in each dimension is 48 times r_{ini} in each simulation. The clouds have an initially spherically symmetric structure, with an isothermal profile out to r_{ini} and a uniform sphere of radius $2 r_{\text{ini}}$ outside that with 0.1 times the density just inside r_{ini} . We apply an initial velocity field with a Kolmogorov power spectrum ($P(k) \propto k^{-5/3}$) with random phases such that the cloud is in approximately virial equilibrium.

2.2 Cloud Evolution and Sink Formation

Each simulation has a root grid of 128^3 cells. We fully refine a sphere of diameter half the box length, encompassing the initial cloud, for two further levels. Gas that exceeds the Jeans criterion by a factor of 10 anywhere in the simulation volume is allowed to refine up to a total of 4 additional levels above the base grid (5 levels in the L cloud). We “relax” each cloud by halving the gravitational forces for one freefall time t_{ff} in order to allow the density and velocity fields to couple.

The sink formation recipe we use is described in detail in Bleuler et al. (2014); Bleuler & Teyssier (2014). We identify clumps above a threshold given by 10% of the Jeans mass in cells at the highest refinement level. If a clump exceeds ten times this threshold, we form a sink particle. Each sink particle accretes 90% of the mass above the sink formation density threshold at each timestep.

2.3 Radiative Transfer and Cooling

We track the advection of ionising photons on the AMR grid using a first-order moment method described in (Rosdahl et al. 2013). We allow the ionising photons to interact with the neutral gas, and track the ionisation states of hydrogen and helium.

We implement the cooling function described in Geen et al. (2016). The cooling in neutral gas is based on Audit & Hennebelle (2005), which includes a background heating term and a fit to Sutherland & Dopita (1993) above 10^4 K. Cooling of photoionised gas is treated as in Rosdahl et al. (2013), with a piecewise fit to Ferland (2003) to describe cooling on photoionised metals.

2.4 UV Source Properties

Each set of initial conditions is run twice, once with no ionising UV photons (labelled “NRT”), and once where ionising UV photons are emitted from sink particles (labelled “RT”). Our resolution is not sufficient to resolve individual stars. Rather, in simulations labelled “RT”, we impose a total hydrogen-ionising photon emission rate of $S_* = (8.96 \times 10^{46}/s)(M_*/M_\odot)$, where M_* is the total mass in sink particles. This is calculated by Monte Carlo sampling a well-sampled stellar population using a Chabrier IMF (Chabrier 2003), with hydrogen-ionising emission rates for each star from Vacca et al. (1996); Sternberg et al. (2003) (see Appendix A in Geen et al. 2016, for further details).

We distribute this total photon emission rate across the sink particles with a weighting $F(qm_i)/\sum_i F(qm_i)$, where m_i is the mass of a given sink particle and $F(m_i)$ is a fit to the photon emission rate for a range of stellar masses given in Vacca et al. (1996); Sternberg et al. (2003). q is a scaling factor that we set to 0.3 as a heuristic to weight emission towards more massive clumps. We adopt this

Cloud Name	$r_{\text{ini}} / \text{pc}^{\text{a}}$	$\Delta x / \text{pc}^{\text{b}}$	$t_{\text{ff}} / \text{Myr}^{\text{c}}$	$n_{\text{sink}} / \text{cm}^{-3}^{\text{d}}$	$\Sigma / M_{\odot} / \text{pc}^2^{\text{e}}$		
					min	median	max
L (Most Diffuse)	7.65	0.03	4.22	9.95×10^5	36.0	41.8	45.1
M (Fiducial)	3.40	0.026	1.25	1.25×10^6	74.5	75.6	87.0
S (More Compact)	1.9	0.014	0.527	3.98×10^6	160.8	175.0	185.5
XS (Most Compact)	0.85	0.0066	0.156	2.01×10^7	540.7	545.2	701.0

Table 1. Cloud properties for each of the sets of initial conditions. ^a Initial cloud radius, excluding envelope. ^b Maximum spatial resolution. ^c The global freefall time of the cloud. Equal to t_{relax} , the length of time for which the cloud is relaxed (see Section 2). ^d Density threshold for sink formation and accretion, equivalent to the Jeans density in cold gas. Clumps are identified above a threshold of $0.1 n_{\text{sink}}$. ^e Mean surface density for pixels above $A_{\text{0.1}}$ taken at t_{ff} . The minimum, median and maximum values are given for values calculated along the three Cartesian axes.

Cloud	Distance / pc
<i>Near</i>	(150)
Taurus	140
Ophiuchus	140
Lupus	140
Chamaeleon-Musca	160
Corona Australis (CrA)	170
<i>Mid</i>	(300)
Aquila Rift	260
Perseus	300
<i>Far</i>	(500)
IC 5146	400
Cepheus	440
Orion	450

Table 2. List of Gould Belt clouds plotted in Figure 2, with distances for each cloud. This list is taken from Planck Collaboration XXXV (2015). The distance bins used in Figure 2 are given in italics, with the distance assumed when calculating the PSF for the simulation results in each bin given in brackets. We use only the Serpents-South region of the Aquila Rift from Herschel.

model, rather than sampling stars using a Monte-Carlo scheme, to avoid stochasticity in the emission rate sampled since this would require a larger sample of simulated clouds to reach convergence.

3 OBSERVATIONS

In this section we describe the set of observations of local clouds used in this work. We compare these clouds' column densities to our simulations in Section 4.1. Comparison is difficult for a number of reasons. Firstly, we must assume that the column densities in our simulations, given as the integrated density down a line of sight in a given Cartesian axis, can be compared to the observed column densities, which are derived as described below. Secondly, our simulations are idealised, isolated setups, which have no environmental dependence. Finally, the samples of simulated clouds and observed clouds are both limited. We cannot comment in this work on whether our results would apply to objects in environments different from the observed clouds listed here.

3.1 Planck

We use maps of each of the Gould Belt objects listed in Planck Collaboration XXXV (2015) (see Table 2). For each object we use the dust optical depth at 353 GHz (τ_{353}) as a proxy for the total gas column density (N_{H}). The τ_{353} map is derived from the all-sky Planck intensity observations at 353, 545, and 857 GHz, and

the IRAS observations at 100 μm , through a modified black body spectrum fit, which also yielded maps of the dust temperature and of the dust opacity spectral index (Planck Collaboration XI 2014). The Planck maps have FWHM of $5'$.

To scale from τ_{353} to N_{H} , following Planck Collaboration XI (2014), we adopted the dust opacity,

$$\sigma_{353} = \tau_{353} / N_{\text{H}} = 1.2 \times 10^{-26} \text{ cm}^2. \quad (1)$$

Variations in dust opacity are present even in the diffuse ISM and the opacity decreases systematically by a factor of 2 from the denser to the diffuse ISM (Planck Collaboration XXIV 2011; Martin et al. 2012; Planck Collaboration XI 2014), but our results do not depend on this calibration.

The maps of the individual regions are projected and resampled onto a Cartesian grid with the gnomonic projection procedure described in Paradis et al. (2012). The present analysis is performed on these projected maps. The selected regions are small enough, and are located at sufficiently low Galactic latitudes that this projection does not impact significantly on our study.

3.2 Herschel

We use the $36''5$ resolution N_{H_2} column density map of the Serpents-South region of the Aquila cloud derived from the 70-, 160-, 250-, 350-, and 500- μm Herschel observations, described in Konyves et al. (2015) and publicly available in the archive of the Herschel Gould Belt Survey¹ (HGBS, André et al. 2010) project. The instrument FWHM is $0.2'$, 25 times smaller than Planck's FWHM.

4 RESULTS

We produce hydrogen column density maps N_{H} for each of our simulation outputs in three lines of sight corresponding to the Cartesian axes using PyMSES², a Python-based tool for analysing RAMSES outputs. For comparison with Lada et al. (2010), we convert N_{H} to extinction A_{k} (in mag) using the relation $N_{\text{H}} = 1.67 \times 10^{22} A_{\text{k}} \text{ cm}^{-2} \text{ mag}^{-1}$ (Lombardi 2008). We display column density maps for L-RT in Figure 1. On each image we plot the position of the sink particles. The fraction of mass accreted in the last 3 Myr, corresponding to the mass in Young Stellar Objects (YSOs), is shown in red. Mass accreted earlier is shown in white. Most of the YSO mass is located within or near gas with column densities higher than $A_{\text{k}} = 0.1 \approx 10^{22} \text{ cm}^{-2}$. We choose a fiducial maximum YSO age $t_{\text{YSO}} = 3 \text{ Myr}$. Note that Lada et al. (2010) use a median YSO age of $2 \pm 1 \text{ Myr}$. Throughout the paper we give errors in t_{YSO} of 1 Myr.

¹ <http://www.herschel.fr/cea/gouldbelt>

² <http://irfu.cea.fr/Projets/PYMSES/>

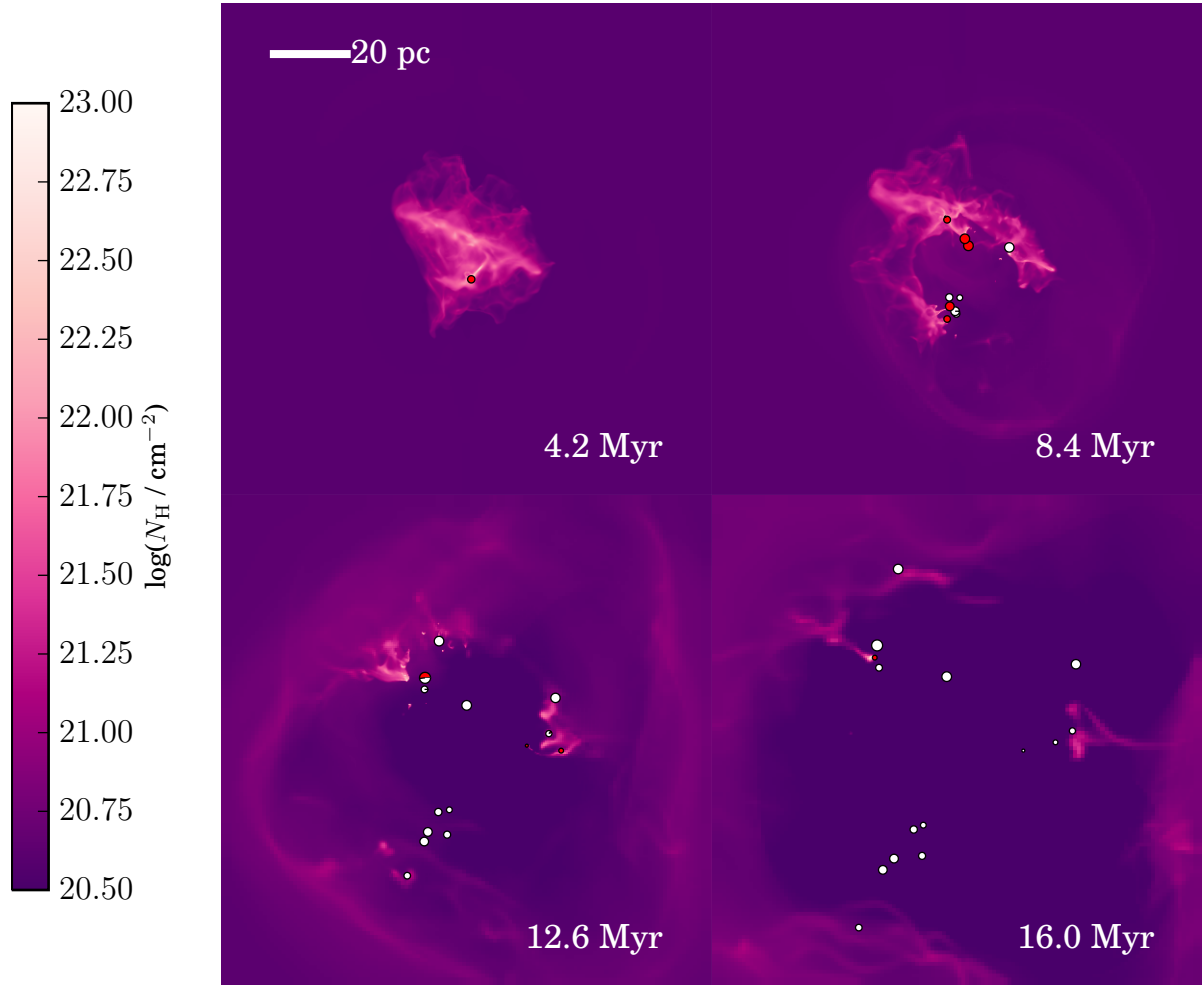


Figure 1. Sequence of hydrogen column density maps in simulation L-RT ($t_{\text{ff}} = 4.2$ Myr). Each sink particle is shown as a pie chart, whose area is proportional to the sink particle mass. The fraction shaded in red captures all of the mass accreted in the last 3 Myr, i.e. the fraction in YSOs.

We also give estimates for the error in column densities found in our simulations by allowing extinction thresholds to vary by $A_{\text{k}} = \pm 0.1$ (± 0.05 if the median A_{k} used is 0.1). We do not create complex synthetic observations of our simulations that reproduce observed column densities in molecular clouds. This is because we lack a sophisticated dust model in our simulations necessary to perform the conversion to column density described in Section 3. We instead assume that these conversions are accurate to within our given errors, and leave deeper comparisons of column density estimates for future work.

As sink particles accrete mass from surrounding dense gas, they produce ionising radiation that disperses the surrounding material by heating the gas to $\sim 10^4$ K, causing the surrounding material to expand and push away infalling matter. This prevents further accretion onto this sink, as well as nearby sinks. Eventually the entire cloud is dispersed, halting star formation globally in the cloud.

There are a number of separate star-forming volumes in our cloud, represented by clusters of sink particles. In panel 2 of Figure 1 at 8.4 Myr, these volumes are found on the edge of the central ionisation front. This might imply that star formation is triggered by the presence of an ionisation front. However, since our star formation

efficiency is reduced by the presence of star formation, we invoke the suggestion of Dale et al. (2015) that these locations would form stars anyway in the absence of an ionisation front. We note that there is no “central” source for the ionising radiation in panel 2. Rather, the sources of ionising radiation follow the expanding shell via gravitational attraction, and the star cluster becomes unbound by 16 Myr.

4.1 Comparisons with Observed Cloud Structure

In Figure 2 we compare the density distribution of material in our clouds against that of the nearby Gould Belt clouds, listed in Table 2. We plot the cumulative mass in bins of descending density for our simulations at t_{ff} and $2t_{\text{ff}}$ as well as the clouds described in Section 3. We convolve our results with a PSF corresponding to the instrument FWHM of $10''$ at three distance bins. These are *Near* at 150 pc, *Mid-range* at 300 pc and *Far* at 500 pc. This removes signal from higher column densities. In the Herschel comparison, we use the Aquila cloud, which is at a distance of 260 pc. The instrument FWHM is $0.2''$, giving a PSF of size 0.06 pc at this distance. This is smaller than the maximum spatial resolution in our simulations. The convolved

density distributions are thus not significantly different from those taken at full resolution. The most diffuse cloud, L, matches the Planck and Herschel results most closely, although cloud M also matches some of the observed clouds at $2 t_{\text{ff}}$.

When the results are taken at full resolution, we are able to detect denser material. Most of the clouds become denser at later times as mass accretes onto dense clumps. These densities can exceed the sink formation threshold since not all of the densest gas is accreted in a single timestep, and the freefall times at these densities are short. This pattern occurs for both column density N_{H} and volume density n_{H} . The only cloud where this is not the case is the run L-RT. Here, HII regions driven by ionising radiation from the sinks creates cavities in the cloud at $2t_{\text{ff}}$ (see Figure 1), reducing the number of pixels with high column densities.

Higher densities are reached in the more compact initial conditions. As well as the initial conditions being denser by construction, the maximum spatial resolution is higher due to the smaller box size. Note that clouds L and M have comparable spatial resolutions. Clouds with the density structure of clouds S and XS are not found in observed local star-forming regions (see Figure 2). In addition, these clouds already have a large quantity of gas above $A_{\text{k}} = 0.8$ ($\approx N_{\text{H}} = 10^{22} \text{ cm}^{-2}$) at $t = 0$, requiring some mechanism to rapidly collect this much gas without forming stars. We posit that extreme environments are needed to create such objects, if indeed it is possible to collect this much dense gas without forming stars.

4.2 Total Star Formation Efficiency

In Figure 3, we plot the total fraction of the initial cloud mass M_{ini} accreted onto sink particles, which we call the Total Star Formation Efficiency (TSFE). M_{ini} is set to $10^4 M_{\odot}$.

In the simulations without radiation, the TSFE tends towards 1 over several t_{ff} for the cloud as a whole (see Table 1). With radiation, the stellar mass reaches a plateau after 1-2 t_{ff} . This plateau corresponds to the time at which the majority of dense gas is dispersed. In the XS simulation, this plateau is never reached due to the density of the cloud preventing ionised outflows (see Geen et al. 2015). In clouds L and M, a number of small plateaus are reached before star formation continues. This corresponds to separate star formation events within the cloud that are ended locally by ionising radiation.

In the NRT simulations, the sink particles accrete continuously over the course of the simulation until the supply of gas is exhausted. In the RT simulations, each sink particle typically accretes during a single burst anywhere between a few hundred kyr to a few Myr. After this time, radiation decouples the sink particle from the dense gas and accretion ends. The mass-weighted mean accretion time is 0.93 Myr in M-RT and 0.47 Myr in L-RT. The median accretion time is 0.63 Myr in M-RT and 0.30 Myr in L-RT. 7 of the 16 sinks in L-RT accrete for less time than the time resolution of our simulation outputs, so this figure is moderately biased towards shorter values. Feedback does not significantly shorten the accretion times in S-RT and XS-RT.

The SFE is roughly 10 times lower when ionising radiation is included than without in the L cloud, 3 times in the M cloud and closer to unity in S and XS. The XS simulations were not completed due to the short timestep in these simulations and their relative cost.

In Figure 9 of Dale et al. (2012), clouds with mass $10^4 M_{\odot}$ and radius above 10 pc do not form stars, while below 3 pc, ionising radiation is ineffective at altering the dynamics of the cloud. Our results are largely in agreement (see Table 1 for initial radii r_{ini}). Clouds L and M both have r_{ini} above 3 pc, and have reduced SFEs.

Cloud L in particular is completely unbound by ionising radiation. Cloud S has an initial radius of 1.9 pc and has some reduction in response to ionising radiation, while Cloud XS ($r_{\text{ini}} = 0.85$) does not respond to ionising radiation at all. Note that since we allow the cloud to relax with half gravity for one freefall time, these initial radii are underestimates of the effective cloud radius at the time stars begin to form.

4.3 Observed Star Formation Efficiency

We now compare our results to observed star formation efficiencies. This quantity is analogous to ϵ in Lada et al. (2010), where $\epsilon = 10 \pm 6\%$. The authors in this paper produce additionally star formation rates per star formation timescale and per freefall time, derived using ϵ . However, since these are quantities with their own uncertainties, we focus on the efficiency to remove sources of uncertainty.

In Figure 4 we plot the Observed Star Formation Efficiency (OSFE) as a function of dense gas mass over time for each of the simulations. OSFE is defined as $M_{\text{YSO}} / M(0.8)$. M_{YSO} is the mass in sinks accreted over the last t_{YSO} , which we choose to be 3 Myr (consistent with Covey et al. 2010; Lada et al. 2010, noting that these authors measure the median and not the maximum YSO age). As in Lada et al. (2010), we include only sink particles inside contours of $A_{\text{k}} = 0.1$ when calculating M_{YSO} . Note that Lada et al. (2010) measure the number of YSOs, N_{YSO} , not the mass. They convert these using a median YSO mass $0.5 M_{\odot}$, i.e. $M_{\text{YSO}} = 0.5 M_{\odot} N_{\text{YSO}}$. $M(0.8)$ is the total mass in all the pixels in the gas column density maps where $A_{\text{k}} > 0.8$. We allow A_{k} to vary by 0.1 and t_{YSO} to vary by 1 Myr, and calculate each quantity for the line of sight along each Cartesian axis. We plot the median value as a solid or dashed line, and the maximum and minimum values as a filled area with the same colour as the line.

We overplot a line at OSFE = 10%, corresponding to the fit to local clouds given in Figure 4 of Lada et al. (2010). Without ionising radiation, the OSFE lies well above this line. The denser clouds have higher star formation efficiencies, although the variation is of the same order as the estimated errors (the shaded areas in Figure 4). With ionising radiation, the OSFE is reduced similarly to the fraction of reduction in the TSFE. In other words, the OSFE is reduced by a factor of 10 in L, 3 in M and just over unity in S. There is, however, more variation due to the age of the YSOs and the variations in dense gas mass.

All of the initial conditions for the clouds contain some gas above $A_{\text{k}} = 0.8$, with the three densest clouds having nearly all of their mass above this threshold. Given this, the gas is rapidly converted into stars. In the denser clouds, where the freefall time is very short, ionising radiation is unable to drive outflows within a short enough time to prevent most of the cloud from being accreted onto sinks. Only the L cloud reaches a quasi-equilibrium state in which the quantity of dense gas plateaus at around $5 \times 10^2 M_{\odot}$.

4.4 Mapping Observed to Total Star Formation Efficiency

In Figure 5 we plot the OSFE given in Figure 4 against the TSFE given in Figure 3. This ratio can be written as

$$\frac{M_{\text{YSO}} M_{\text{ini}}}{M(A_{\text{k}}) M_{*}} \quad (2)$$

where M_{YSO} is the mass in YSOs. There is no clear 1:1 mapping between the two quantities. OSFE measured for gas above $A_{\text{k}} = 0.1$ (right panel) is similar to TSFE at first to within a factor of a few, although it drops at late times as populations of stars age and are no

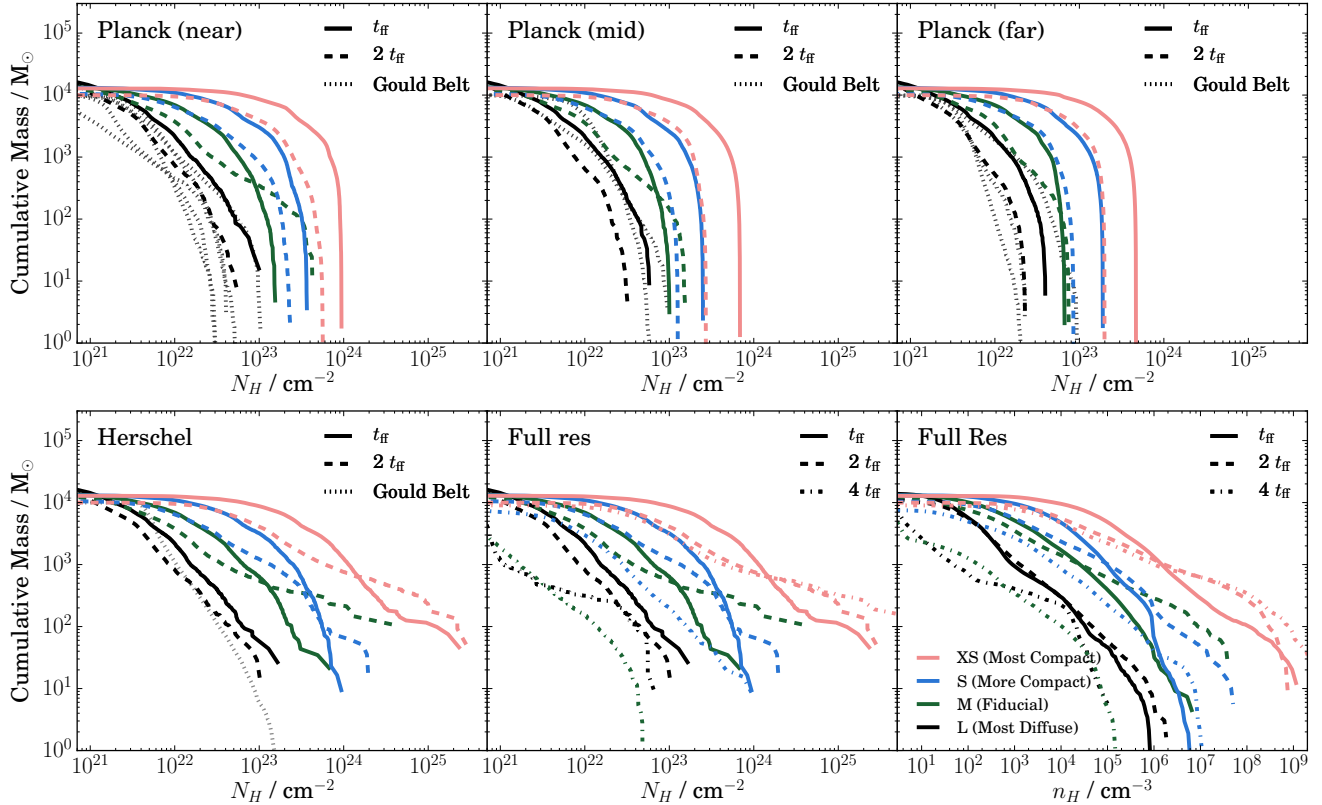


Figure 2. Cumulative density distributions in each of the simulations including ionising radiation, i.e. L-RT, M-RT, S-RT and XS-RT, with comparison to Planck and Herschel maps of Gould Belt objects (see Table 2 and Section 3). The top panels show cumulative column density distributions of our simulations at t_{ff} (solid line), and $2 t_{\text{ff}}$ (dashed line), and Planck data in groups of nearby (left, 150 pc), mid-range (centre, 300 pc) and far (right, 500 pc). Planck data is given as a grey dotted line. Each of the simulation results in the top panels is convolved with the Planck PSF, with FWHM of $5'$. In each panel we assume our simulated clouds are at the distance given previously. In the left lower panel, we perform the same comparison with the Aquila region in Herschel. The FWHM here is $0.2'$, which gives a PSF smaller than our simulations' resolution (see Section 4.1). In the centre lower panel, we show the cumulative column density distribution of our simulations with no PSF applied. In the right lower panel we show the cumulative volume density distribution of our simulations. In these last two panels we also include our simulations results at $4 t_{\text{ff}}$ (dash-dot line), or the final output in the simulation, whichever is earlier.

longer identified as YSOs. Meanwhile, the OSFE for $A_k = 0.8$ (left panel) is roughly 10 times larger than the TSFE since there is less gas above this threshold than the total cloud mass of $10^4 M_\odot$ (see the lower panel of Figure 4). It is thus not immediately clear that values such as the total amount of a cloud converted into stars can be trivially derived from observed quantities.

In Figure 6 we allow the ratio $\text{OSFE}(A_k) / \text{TSFE}$ to vary with A_k . There is a large degree of variation in the results at each value of A_k due to variation with time. The results for XS-RT are roughly constant since nearly all of the gas is above $A_k = 1$ ($N_H \approx 10^{23} \text{ cm}^{-2}$, see Figure 2). The median values for the other simulations follow a roughly similar trend above $A_k \approx 0.4$. This suggests that any value of A_k above this limit can be used to produce a convergent star formation efficiency.

We find a systematic trend to higher values of $\text{OSFE}(A_k)/\text{TSFE}$ for increasing A_k . This is because the amount of mass in gas above a certain value of A_k drops as A_k increases (see Equation 2). Since $M(A_k)$ is typically smaller than M_{ini} (see Figure 4), the ratio $\text{OSFE}(A_k)/\text{TSFE}$ can be over 1 for larger values of A_k .

All of the simulations display at least a factor of ten variation in OSFE/TSFE over time for a given value of A_k . This makes an exact conversion from OSFE to TSFE difficult. Some time variation can be accounted for by studying the time evolution of the stellar populations and HII regions (see, e.g., Tremblin et al. 2014). Older

clusters exhibit a smaller OSFE/TSFE, since the number of YSOs is truncated at 3 Myr, while the TSFE includes all stars formed by the cloud.

4.5 Likelihood of Observing a Given SFE

In Figure 7 we plot the YSO mass M_{YSO} against the mass of gas above $A_k = 0.8$, $M(0.8)$, for each of the simulations with ionising radiation included. We interpolate the values of each quantity to intervals of 0.2 Myr in order to obtain the probability of observing the cloud in a given state. We overplot the same fit to Lada et al. (2010), $M_{\text{YSO}} = 0.1 M(0.8)$, given in Section 4.3.

All of the clouds start at high $M(0.8)$ and low M_{YSO} . They rapidly reach a peak M_{YSO} , before tailing off to low values of M_{YSO} and $M(0.8)$ as the supply of dense gas is depleted (see Figure 4). In cloud L, in the late phase of the cloud's evolution, M_{YSO} drops rapidly while $M(0.8)$ remains constant. This suggests that it is possible to accumulate supply of dense gas that is relatively quiescent in clouds that have been recently star-forming. Looking at the lower right panel of Figure 2, the maximum gas volume density at $4 t_{\text{ff}}$ is below the threshold for forming stars in clouds L and M, despite the presence of gas above 10^{22} cm^{-2} . Since YSOs have a maximum age (3 ± 1 Myr) longer than the typical accretion time

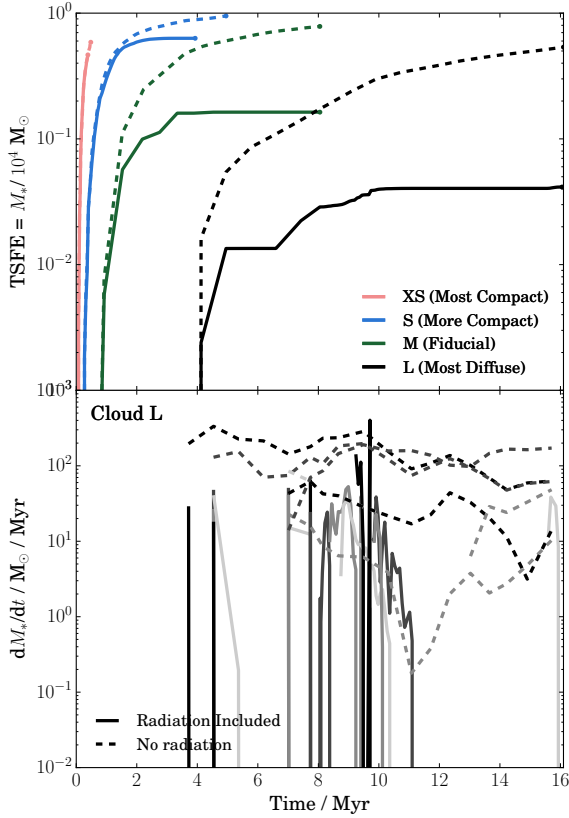


Figure 3. Top: Total star formation efficiency of each simulation over time, measured as the total mass in stars divided by the initial cloud mass. Each initial cloud density is coloured according to the legend. Simulations without radiation are shown as a dashed line, and simulations with radiation as a solid line. Bottom: The corresponding mass accretion rate over time for each particle in the L cloud setup (i.e. the most diffuse). The shades of grey alternate for each sink particle to highlight their individual accretion histories.

onto a protocluster (0.1 to 1 Myr), the presence of a YSO is not a guarantee that stars are still actively forming in a particular volume.

Our L cloud, which most closely represents the Gould Belt clouds’ density distribution (see Section 4.1), matches the fit of Lada et al. (2010) to within the estimated spread in M_{YSO} and $M(0.8)$. The initial phase of star formation is rapid, and so is less likely to be observed than the main sequence of the evolution. Finally, the late phase of cloud dispersal and minimal star formation is not sampled by the Gould Belt objects owing to their ages. The low number of nearby clouds and the limited sample of simulated clouds in this study prevents a more statistical comparison.

In addition to being less similar to local clouds, the denser clouds in our simulations live for shorter times. The most compact, XS, is only sampled for one point on our curve, by chance on the Lada et al. (2010) fit. Even if these clouds are formed in equal numbers with more diffuse clouds, we expect them to be detected in fewer numbers due to their shorter lifespans.

5 DISCUSSION

In our work we reproduce observed star formation efficiencies, but only for clouds similar to local clouds (L and, to some extent, M, in our study). Our cloud most similar to local observed clouds plateaus

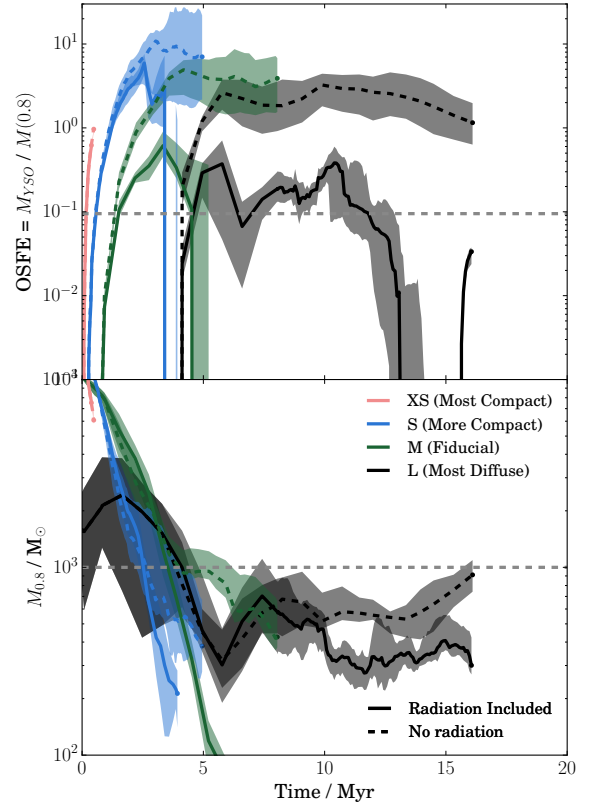


Figure 4. Top: The “observed” star formation efficiency OSFE in dense gas for each cloud over time, calculated as the mass in YSOs M_{YSO} divided by the mass in dense gas $M(0.8)$. M_{YSO} is the mass in sink particles inside contours of $A_k = 0.1$ accreted in the last $t_{\text{YSO}} = 3$ Myr. $M(0.8)$ is the total mass in pixels above $A_k = 0.8$. Errors are given for $t_{\text{YSO}} = [2, 4]$ Myr and $A_k = [0.7, 0.9]$ as filled regions of the same colour. Bottom: $M(0.8)$ over time, with filled areas showing the total mass in gas between $A_k = 0.7$ and 0.9 .

at an OSFE of 0.1 (similar to Lada et al. 2010) for 2–3 t_{ff} before the densest gas is depleted. Once the densest gas is depleted, we still find gas above $A_k = 0.8$ that is not star-forming. Since protoclusters form over a very short period of time (0.1 to 1 Myr), sampling stars below $t_{\text{YSO}} = 3$ Myr acts as a smoothing window that captures recent as well as ongoing star-formation events. This helps provide a smoother signal for $M_{\text{YSO}}/M(0.8)$, while the instantaneous star formation rate can be highly bursty (see Figure 3).

Producing a model for the self-regulation of star formation in clouds that accurately describes all the important processes is an extremely challenging task and one that is beyond the scope of this paper. However, it is clear that energetic stellar processes that reverse gas infall around protoclusters are an important dynamical process in setting the star formation efficiencies of molecular clouds, regardless of the details of how such processes behave and interact with the cloud.

There are a number of limitations to this work. Our numerical resolution does not allow us to treat each sink as an individual star, and hence our model for ionising radiation output is relatively simple. We also neglect processes such as stellar winds, protostellar outflows, radiation pressure and supernovae. More sophisticated models and higher resolution are needed to increase the physical fidelity of our results and allow closer comparison to observations. In addition, for star clusters below $10^4 M_\odot$, we do not expect the

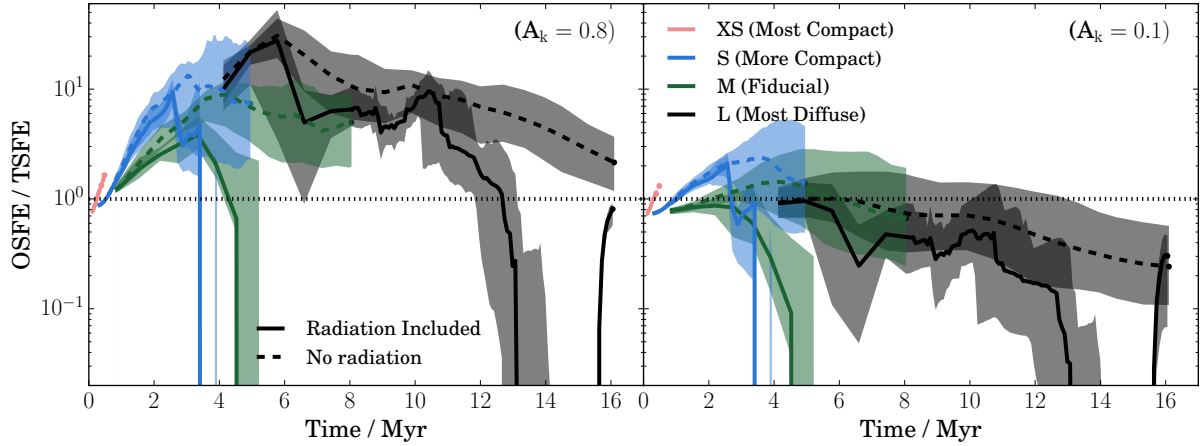


Figure 5. Ratio between OSFE and TSFE over time in each of the simulations. OSFE is defined as the YSO mass divided by the mass in pixels above a given extinction threshold A_k . TSFE is defined as the total mass in stars divided by the initial mass of the cloud, $10^4 M_\odot$. On the left we show this quantity for an extinction limit $A_k = 0.8$, representing on the dense gas, and on the right we show $A_k = 0.1$, which captures the majority the cloud material. The horizontal dotted line is where OSFE=TSFE.

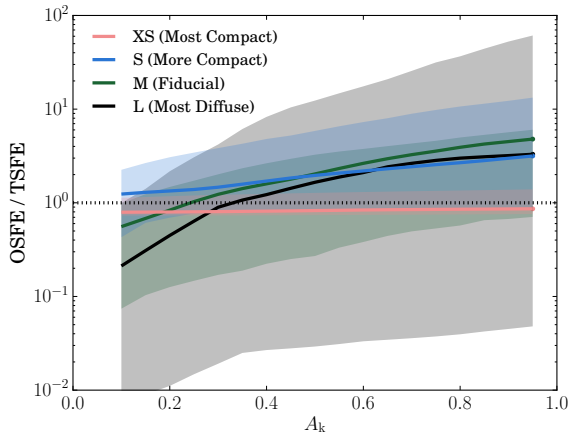


Figure 6. $OSFE(A_k) / TSFE$ in each of the simulations containing radiation (labelled “-RT”) versus A_k . Each colour corresponds to a different simulation. The filled areas are the range between maximum and minimum values at each A_k for each time, Cartesian projection and value of t_{YSO} defined in Section 4.3, excluding values where either OSFE or TSFE are zero. The solid line is the median value for each of these. The dotted line is the ratio where OSFE = TSFE.

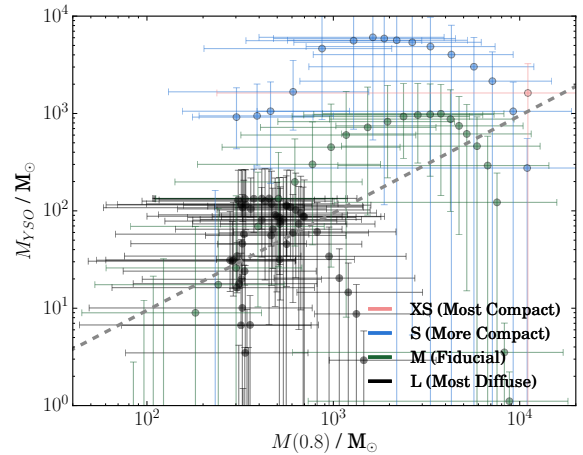


Figure 7. YSO mass, M_{YSO} , vs mass in gas above $A_k = 0.8$, $M(0.8)$, for each simulation sampled at uniform time intervals. The YSO ages t_{YSO} is 3 Myr. Error bars are given for $t_{YSO} = [2, 4]$ Myr and $A_k = [0.7, 0.9]$. Cloud properties are linearly interpolated between snapshots to uniform intervals of 0.2 Myr in order to illustrate the probability of observing a cloud at each given point in its evolution. The dashed line is the fit to Lada et al. (2010) using their conversion factor between N_{YSO} and M_{YSO} of $0.5 M_\odot$.

Initial Mass Function (IMF) to be fully sampled (see Appendix A of Geen et al. 2016). This means that more simulations will be needed to properly sample the range of possible ionising photon emission rates for a given cluster mass.

We do not address directly in this work the origin of molecular clouds or any environmental effects that influence molecular cloud formation and destruction. Instead, we invoke starless clouds of a certain density *ab initio*. In the initial conditions of our denser clouds, M, S and XS, nearly all of the mass is in gas identified in the dense phase (above $A_k = 0.8$ or $N_H = 10^{22} \text{ cm}^{-2}$). This means that stars are able to form rapidly before ionising radiation is able to disperse the host cloud. Larger-scale studies that describe the formation of molecular clouds in various conditions are needed to determine whether collecting such a large quantity of starless cloud material is physical.

6 CONCLUSIONS

We use radiative magnetohydrodynamic simulations with self-consistent star formation and ionising radiation from massive stars to explore the origins of observed local star formation relations. Energetic processes from massive stars drive outflows in the gas around them and end star formation in the volume around them.

We simulate a series of isolated clouds of various initial densities with and without ionising radiation. We compare the cumulative density probability distribution function (PDF) of these clouds to local clouds in the Milky Way by convolving our column density maps with the appropriate point spread function (PSF). We find that the more diffuse clouds in our sample most closely represent the observed clouds. This suggests that the densest clouds are either unphysical, or are more similar to clouds in different environments than in the Galactic neighbourhood.

We then compute the star formation efficiency (SFE) of each cloud. We define two measures of SFE. Firstly, we measure the total fraction of the initial cloud mass converted to stars, the “Total” SFE (TSFE). Secondly, we define an observationally-motivated SFE measurement, which we call OSFE. This is the mass in YSOs, measured as the mass recently accreted onto sink particles, divided by the gas mass in pixels above a given column density threshold. The clouds most similar to nearby molecular clouds reproduce the OSFE found by authors such as Lada et al. (2010).

Without ionising radiation, the TSFE tends to 100% over several freefall times. When ionising radiation is included, the TSFE drops. In the clouds most similar to local star-forming clouds, we find a TSFE of a few percent. The OSFE is typically 3 to 10 times higher than the TSFE, depending on the density threshold used. We discuss the possibility for deriving a TSFE from the OSFE. It is not trivial to do this for a number of reasons, and care should be taken directly comparing the two. However, there is a relation between OSFE and TSFE for a given column density or extinction threshold, albeit with a large error.

7 ACKNOWLEDGEMENTS

We thank Andreas Bleuler, Simon Glover, Sacha Hony, Ralf Klessen, Eric Pellegrini, Joakim Rosdahl and Romain Teyssier for their useful comments and discussions during the preparation of this work. This work was granted access to HPC resources of CINES under the allocation x2014047023 made by GENCI (Grand Equipement National de Calcul Intensif). This work has been funded by the the European Research Council under the European Community’s Seventh Framework Programme (FP7/2007-2013). All three authors have received funding from Grant Agreement no. 306483 of this programme. SG has received additional funding from Grant Agreement no. 339177 (STARLIGHT). JS has received additional funding from Grant Agreement no. 291294.

REFERENCES

- André P., et al., 2010, *Astron. Astrophys. Vol. 518*, id.L102, 7 pp., 518
- Audit E., Hennebelle P., 2005, *Astron. Astrophys.*, 433, 1
- Beichman C. A., Myers P. C., Emerson J. P., Harris S., Mathieu R., Benson P. J., Jennings R. E., 1986, *Astrophys. J.*, 307, 337
- Bertoldi F., McKee C. F., 1990, *Astrophys. J.*, 354, 529
- Bleuler A., Teyssier R., 2014, *Mon. Not. R. Astron. Soc. Vol. 445*, Issue 4, p.4015-4036, 445, 4015
- Bleuler A., Teyssier R., Carassou S., Martizzi D., 2014, *Comput. Astrophys. Cosmol. Vol. 2*, Artic. id.5, 16 pp., 2
- Burkert A., Hartmann L., 2013, *Astrophys. Journal*, Vol. 773, Issue 1, Artic. id. 48, 10 pp. (2013)., 773
- Chabrier G., 2003, *Publ. Astron. Soc. Pacific*, 115, 763
- Clark P. C., Glover S. C. O., 2014, *Mon. Not. R. Astron. Soc. Vol. 444*, Issue 3, p.2396-2414, 444, 2396
- Covey K. R., Lada C. J., Roman-Zuniga C., Muench A. A., Forbrich J., Ascenso J., 2010, *Astrophys. Journal*, Vol. 722, Issue 2, pp. 971-988 (2010)., 722, 971
- Dale J. E., 2015, *Phys. Rev. B*, 68, 1
- Dale J. E., Bonnell I. A., Clarke C. J., Bate M. R., 2005, *Mon. Not. R. Astron. Soc.*, 358, 291
- Dale J. E., Ercolano B., Bonnell I. A., 2012, *Mon. Not. R. Astron. Soc.*, 424, 377
- Dale J. E., Haworth T. J., Bressert E., 2015, *Mon. Not. R. Astron. Soc.*, 450, 1199
- Dyson J., Williams D., 1997, *The physics of the interstellar medium*. Vol. 2008
- Ferland G. J., 2003, *Annu. Rev. Astron. Astrophys.*, 41, 517
- Fromang S., Hennebelle P., Teyssier R., 2006, *Astron. Astrophys.*, 457, 371
- Geen S., Hennebelle P., Tremblin P., Rosdahl J., 2015, *Mon. Not. R. Astron. Soc.*, 454, 4484
- Geen S., Hennebelle P., Tremblin P., Rosdahl J., 2016, *Mon. Not. R. Astron. Soc. Vol. 463*, Issue 3, p.3129-3142, 463, 3129
- Goldbaum N. J., Krumholz M. R., Matzner C. D., McKee C. F., 2011, *Astrophys. J.*, 738, 101
- Gritschneider M., Naab T., Walch S., Burkert A., Heitsch F., 2009, *Astrophys. J.*, 694, L26
- Gutermuth R. A., Pipher J. L., Megeath S. T., Myers P. C., Allen L. E., Allen T. S., 2011, *Astrophys. Journal*, Vol. 739, Issue 2, Artic. id. 84, 17 pp. (2011)., 739
- Heiderman A., Evans N. J., Allen L. E., Huard T., Heyer M., 2010, *Astrophys. Journal*, Vol. 723, Issue 2, Artic. id. 1019-1037 (2010)., 723
- Hennebelle P., Falgarone E., 2012, *Astron. Astrophys. Rev.*, 20, 55
- Hony S., et al., 2015, *Mon. Not. R. Astron. Soc. Vol. 448*, Issue 2, p.1847-1862, 448, 1847
- Hosokawa T., Inutsuka S., 2006, *Astrophys. J.*, 646, 240
- Johnstone D., Di Francesco J., Kirk H., 2004, *Astrophys. Journal*, Vol. 611, Issue 1, pp. L45-L48., 611, L45
- Kim J.-G., Kim W.-T., Ostriker E. C., 2016, *Astrophys. J.*, 819, 23
- Konyves V., et al., 2015, *Astron. Astrophys. Vol. 584*, id.A91, 33 pp., 584
- Krumholz M. R., Matzner C. D., McKee C. F., 2006, *Astrophys. Journal*, Vol. 653, Issue 1, pp. 361-382., 653, 361
- Krumholz M. R., Dekel A., McKee C. F., 2012, *Astrophys. J.*, 745, 69
- Lada C. J., Lombardi M., Alves J. F., 2010, *Astrophys. J.*, 724, 687
- Lee Y.-N., Hennebelle P., 2016, *Astron. Astrophys.*, 30, 1
- Lombardi M., 2008, *Astron. Astrophys. Vol. 493*, Issue 2, 2009, pp.735-745, 493, 735
- Martin P. G., et al., 2012, *Astrophys. Journal*, Vol. 751, Issue 1, Artic. id. 28, 14 pp. (2012)., 751
- Matzner C. D., 2002, *Astrophys. J.*, 566, 302
- Myers P. C., Benson P. J., 1983, *Astrophys. J.*, 266, 309
- Onishi T., Mizuno A., Kawamura A., Ogawa H., Fukui Y., 1998, *Astrophys. J.*, 502, 296
- Paradis D., Dobashi K., Shimoikura T., Kawamura A., Onishi T., Fukui Y., Bernard J. P., 2012, *Astron. Astrophys. Vol. 543*, id.A103, 9 pp., 543
- Peters T., Banerjee R., Klessen R. S., Low M.-M. M., Galván-Madrid R., Keto E. R., 2010, *Astrophys. J.*, 711, 1017
- Planck Collaboration XXIV 2011, *A&A*, 536, A24
- Planck Collaboration XI 2014, *A&A*, 571, A11
- Planck Collaboration XXXV 2015, *Astron. Astrophys. Vol. 586*, id.A138, 29 pp., 586
- Raga A. C., Canto J., Rodriguez L. F., 2012, *Mon. Not. R. Astron. Soc.*, 419, L39
- Rosdahl J., Blaizot J., Aubert D., Stranex T., Teyssier R., 2013, *Mon. Not. R. Astron. Soc.*, 436, 2188
- Spitzer L., 1978, *Physical processes in the interstellar medium*
- Sternberg A., Hoffmann T. L., Pauldrach A. W. A., 2003, *Astrophys. J.*, 599, 1333
- Sutherland R. S., Dopita M. A., 1993, *Astrophys. J. Suppl. Ser.*, 88, 253
- Teyssier R., 2002, *Astron. Astrophys.*, 385, 337
- Tremblin P., et al., 2014, *Astron. Astrophys.*, 568, A4
- Vacca W. D., Garmany C. D., Shull J. M., 1996, *Astrophys. J.*, 460, 914
- Walch S. K., Whitworth A. P., Bisbas T., Wünsch R., Hubber D., 2012, *Mon. Not. R. Astron. Soc.*, 427, 625
- Whitworth A., 1979, *Mon. Not. R. Astron. Soc.*, 186, 59